SLAC-PUB-12814
astro-ph/0709.1162
September 2007

Last revision September 7, 2007.
Preprint typeset using LaTeX style emulateapj v. 03/07/07

CROSS-CORRELATION WEAK LENSING OF SDSS GALAXY CLUSTERS III: MASS-TO-LIGHT RATIOS

Erin S. Sheldon,[1] David E. Johnston,[2,3] Morad Masjedi,[1] Timothy A. McKay,[4,5,6] Michael R. Blanton,[1] Ryan Scranton,[7] Risa H. Wechsler,[8] Ben P. Koester,[9,10] Sarah M. Hansen,[9,10] Joshua A. Frieman,[9,10,11] and James Annis[11]

Last revision September 7, 2007.

ABSTRACT

We present measurements of the excess mass-to-light ratio measured around MaxBCG galaxy clusters observed in the SDSS. This red sequence cluster sample includes objects from small groups with $M_{200} \sim 5 \times 10^{12} h^{-1} M_\odot$ to clusters with $M_{200} \sim 10^{15} h^{-1} M_\odot$. Using cross-correlation weak lensing, we measure the excess mass density profile above the universal mean $\Delta\rho(r) = \rho(r) - \bar{\rho}$ for clusters in bins of richness and optical luminosity. We also measure the excess $^{0.25}i$-band luminosity density $\Delta\ell(r) = \ell(r) - \bar{\ell}$. For both mass and light, we de-project the profiles to produce 3D mass and light profiles over scales from $25h^{-1}$ kpc to $22h^{-1}$ Mpc. From these profiles we calculate the cumulative excess mass $\Delta M(r)$ and excess light $\Delta L(r)$ as a function of separation from the BCG. On small scales, where $\rho(r) \gg \bar{\rho}$, the integrated mass-to-light profile $(\Delta M/\Delta L)(r)$ may be interpreted as the cluster mass-to-light ratio. We find the $(\Delta M/\Delta L)_{200}$, the mass-to-light ratio within r_{200}, scales with cluster mass as a power law with index 0.33 ± 0.02. On large scales, where $\rho(r) \sim \bar{\rho}$, the $\Delta M/\Delta L$approaches an asymptotic value independent of scale or cluster richness. For small groups, the mean $(\Delta M/\Delta L)_{200}$ is much smaller than the asymptotic value, while for large clusters $(\Delta M/\Delta L)_{200}$ is consistent with the asymptotic value. This asymptotic value should be proportional to the mean mass-to-light ratio of the universe $\langle M/L \rangle$. We find $\langle M/L \rangle\ b_{M/L}^{-2} = 362 \pm 54h$ measured in the $^{0.25}i$-bandpass. The parameter $b_{M/L}^2$ is primarily a function of the bias of the $L \lesssim L_*$ galaxies used as light tracers, and should be of order unity. Multiplying by the luminosity density in the same bandpass we find $\Omega_m b_{M/L}^{-2} = 0.20 \pm 0.03$, independent of the Hubble parameter.

Subject headings: dark matter — galaxies: clusters: general — gravitational lensing — large-scale structure of the universe

1. INTRODUCTION

Comparison of luminous to total mass through the mass-to-light ratio (M/L) dates back at least to Kapteyn (1922), who found values of $\mathrm{M/L} \sim 2\ \mathrm{M}_\odot/\mathrm{L}_\odot$ in the solar neighborhood. Similar values were found by Hubble for the disk of Andromeda in 1929 (Hubble 1929). Extension of this approach to larger scales was first attempted by Zwicky in 1933 for the Coma cluster (Zwicky 1933, 1937). Under reasonable assumptions about the cluster's dynamical state, Zwicky estimated the mass of the cluster. The inferred average M/L for cluster galaxies was around 500 $\mathrm{M}_\odot/\mathrm{L}_\odot$, implying a surprising dominance of dark over luminous matter.

Decades of observation confirm Zwicky's conclusion that dark matter dominates on large scales. The simplest model capable of accommodating current observations is the Cold Dark Matter (CDM) model. It assumes that approximately 80% of the cosmic mass density is in the form of some dynamically cold, collisionless species of subatomic particle. Monte Carlo predictions for the evolution of structure in such a CDM universe have reached a high level of sophistication. Given a set of cosmological parameters and initial conditions, modern simulations are accurate and predictive within well understood limitations imposed by resolution and simulation volume (see e.g. the comparison paper of Heitmann et al. 2007, and references therein). However, accurate simulations of the baryonic components of clusters remain beyond both current theoretical understanding and simulation technology. Absent direct theoretical prediction, observations of the connection between observable light and computable dark matter remain important. The simplest connection, still relevant 90 years after Kapteyn, is the mass-to-light ratio.

Observations of both mass and light have advanced considerably since Zwicky's time. Dynamics of cluster galaxies still provide important constraints on cluster masses. These have confirmed Zwicky's essential conclusions with much better accuracy over a broader range of environments (e.g. Carlberg, Yee, & Ellingson 1997).

[1] Center for Cosmology and Particle Physics, Department of Physics, New York University, 4 Washington Place, New York, NY 10003.
[2] Department of Astronomy, 105-24, California Institute of Technology, 1201 East California Boulevard, Pasadena, CA 91125.
[3] Jet Propulsion Laboratory 4800 Oak Grove Drive, Pasadena ,CA, 91109
[4] Department of Physics, University of Michigan, 500 East University, Ann Arbor, MI 48109-1120.
[5] Department of Astronomy, University of Michigan, 500 Church St., Ann Arbor, MI 48109-1042
[6] Michigan Center for Theoretical Physics, University of Michigan, 500 Church St., Ann Arbor, MI 48109-1042
[7] Department of Physics and Astronomy, University of Pittsburgh, 3941 O'Hara Street, Pittsburgh, PA 15260.
[8] Kavli Institute for Particle Astrophysics & Cosmology, Physics Department, and Stanford Linear Accelerator Center, Stanford University, Stanford, CA 94305
[9] Kavli Institute for Cosmological Physics, The University of Chicago, 5640 South Ellis Avenue Chicago, IL 60637
[10] Department of Astronomy and Astrophysics, The University of Chicago, 5640 South Ellis Avenue, Chicago, IL 60637.
[11] Fermi National Accelerator Laboratory, P.O. Box 500, Batavia, IL 60510.

There are also new analysis techniques such as the "caustics" method (Rines et al. 2004) and velocity stacking methods (e.g Becker et al. 2007) which confirm and extend the standard analyses.

The X–ray emission from the hot intracluster plasma has become a favored proxy for cluster mass. Under similar assumptions of hydrostatic equilibrium, masses and mass-to-light ratios can be calculated from X-ray temperatures and, less directly, luminosities. These X-ray analyses confirm the dynamical measurements of high mass-to-light ratios (e.g. Lin, Mohr, & Stanford 2004).

Weak gravitational lensing, an effect which Zwicky thought promising (Zwicky 1937), is now an established technique for studying the mass distributions in clusters of galaxies. The effect, deflection of light from background objects as it passes foreground clusters, is generally less precise on a cluster-by-cluster basis than X–ray or velocity measurements. But it is complementary in that it is independent of the dynamical state of the system, is linear in the density, and can be measured at a large range of separations from the cluster center.

Weak lensing studies have traditionally focused on measuring the mass of individual clusters[12]. However, averaging the lensing signal over many clusters is more robust and easier to interpret (see the discussions in Johnston et al. 2007a; Sheldon et al. 2007; Johnston et al. 2007b). With this method, the full M/L profile can be measured from small scales to well beyond the bound regions of the clusters. Early stacked M/L results (Hoekstra et al. 2001; Parker et al. 2005, e.g.) showed the promise of this approach. The pilot study of Sheldon et al. (2001) demonstrated the great potential of the Sloan Digital Sky Survey (SDSS; York et al. 2000) for measuring cluster masses.

In this work we measure the mean mass-to-light ratios for SDSS groups and clusters drawn from the MaxBCG cluster sample (Koester et al. 2007a,b). We compare the ensemble mass estimates from the first two papers in this series (Sheldon et al. 2007; Johnston et al. 2007b) with ensemble measurements of the total light. We measure the mean mass using lensing, and the mean luminosity by correlating the clusters with the surrounding galaxies. Each measurement spans a range of separations from $25h^{-1}$kpc to $22h^{-1}$Mpc, extending the volume over which the M/L is measured well beyond the virial radii of the clusters.

Because lensing is not sensitive to uniform mass distributions, aka "mass sheets", we measure the mean mass density of a lens sample above the mean density of the universe $\Delta\rho$=$\rho(r) - \bar{\rho}$ (actually we measure a 2D projection of the 3D $\Delta\rho$ which we will de-project). In other words, we measure the cluster-mass cross correlation function times the mean density of the universe $\Delta\rho = \bar{\rho}\xi_{cm}$. On small scales this is a measure of the mean density profile, but on large scales, where the density approaches the background, it can only be interpreted in terms of the correlation function.

To measure the light we use a stacking technique directly comparable to the lensing measurements. We measure the total light from all galaxies down to some luminosity threshold around the clusters and then subtract the measurements around random points in order to remove the uniform background. This means we measure the luminosity density above the mean $\Delta\ell = \ell(r) - \bar{\ell}$, so it is a correlation function just like the mass measurement . The excess mass within radius r divided by the excess luminosity within radius r is the ratio of integrals of correlation functions:

$$\frac{\Delta M}{\Delta L}(<r) = \frac{\int_0^r \mathrm{d}r\,[\,\rho(r) - \bar{\rho}\,]\;r^2}{\int_0^r \mathrm{d}r\,[\,\ell(r) - \bar{\ell}\,]\;r^2} = \frac{\int_0^r \mathrm{d}r\;\bar{\rho}\;\xi_{cm}\;r^2}{\int_0^r \mathrm{d}r\;\bar{\ell}\;\xi_{c\ell}\;r^2}. \quad (1)$$

On the scale of virialized halos, defined where the mean density is a few hundred times the mean, equation 1 can be interpreted as the mean cluster M/L in a straightforward way. On very large scales, as the density approaches the mean, equation 1 becomes proportional to the mean mass-to-light ratio of the universe. The proportionality constant is related to the particulars of the correlation function measurements. For example, the light and mass may be clustered differently , and this difference may depend on the properties of the galaxies chosen as tracers of the light. Thus we expect this measurement to depend on the "bias" of the light tracers relative to the mass. This bias depends primarily on the mass of the halos hosting these tracers. The bias depends secondarily on the variance of the mass density field (σ_8) as the larger the variance in that field the smaller the bias at fixed mass.

Full theoretical models of this measurement on all scales will require substantial effort. For this paper we will parametrize our ignorance at large scales in terms of the bias. We will write the asymptotic M/L as

$$(\Delta M/\Delta L)_{asym} = \langle M/L\rangle\; b_{M/L}^{-2}$$
$$b_{M/L}^{-2} = \frac{b_{cm}}{b_{c\ell}}\frac{1}{b_{\ell m}^2}. \quad (2)$$

Here $\langle M/L\rangle$ is the mean mass-to-light ratio of the universe, but it is multiplied by a bias factor $b_{M/L}^{-2}$. This factor depends on the bias of the galaxy tracers relative to the mass $b_{\ell m}$, which should be of order unity for tracers near L_* since these galaxies are expected to be only slightly anti-biased (Sheth & Tormen 1999; Seljak & Warren 2004). This term also depends on the ratio of the bias of clusters relative to mass and light $b_{cm}/b_{c\ell}$, which should also be near unity for the same reasons. The cluster bias is likely to cancel from this equation because the cluster terms appear in a ratio $b_{cm}/b_{c\ell}$.

On large enough scales, $\Delta M/\Delta L$ should approach a constant value independent of the halo mass as long as the bias of the light tracers, and thus $b_{M/L}^2$, is equivalent in all cases. This appears to be the case, as we will demonstrate.

The notation may get confusing due to the use of multiple apertures in the course of cluster finding and lensing measurements. The basic notation for cluster variables is the same as Sheldon et al. (2007): the measures of richness and luminosity we will refer to as N_{200} and L_{200}. These are the counts and i-band luminosity for galaxies with $L_i > 0.4L_*$, colors consistent with the cluster

[12] A few examples: Fahlman et al. (1994); Tyson & Fischer (1995); Luppino & Kaiser (1997); Fischer & Tyson (1997); Hoekstra et al. (1998); Joffre et al. (2000); Clowe et al. (2000); Dahle et al. (2002); Wittman et al. (2003); Umetsu et al. (2005); Clowe et al. (2006).

ridge-line, and projected separation less than r_{200}^{gals} as calibrated in Hansen et al. (2005). This radius is different from the radius r_{200}^{mass} calculated from the mass profile, which is typically half as big. The L_{200} is only used for binning the clusters; because the results are the same for L_{200} and N_{200} binning we will avoid using the L_{200} notation except where necessary. We refer to the total excess luminosity, which includes the light of all types of galaxies above a luminosity threshold, as $\Delta L(r)$. This luminosity, and excess mass $\Delta M(r)$, are the new measurements presented in this paper. The total excess mass and light within r_{200}^{mass} are denoted ΔM_{200} and ΔL_{200}. Projected 2D radii are referred to as R and 3D radii are referred to as r.

We assume a Friedman-Robertson-Walker cosmology with $\Omega_M = 0.27$, $\Omega_\Lambda = 0.73$, and $\mathrm{H}_0 = 100\ h$ km/s/Mpc and distances are measured in physical, or proper units, rather than comoving units.

2. METHODS

2.1. *Lensing Methods*

We will briefly describe the lensing measurements as these were described in detail in Sheldon et al. (2007) and Johnston et al. (2007b). We measure the tangential shear induced in background galaxies by a set of foreground clusters and convert that shear to a redshift independent density contrast $\Delta\Sigma$:

$$\gamma_T(R) \times \Sigma_{crit} = \bar{\Sigma}(< R) - \bar{\Sigma}(R) \equiv \Delta\Sigma\ , \qquad (3)$$

where $\bar{\Sigma}$ is the projected surface mass density at radius R and $\bar{\Sigma}(< R)$ is the mean projected density within radius R. In using this equation, we assume the shear is weak. This is not always the case for the largest clusters on the smallest scales; we will discuss this in more detail in the results section (§9).

We average $\Delta\Sigma$ for an ensemble of clusters in radial bins from $25h^{-1}$kpc to $30h^{-1}$Mpc, using the brightest cluster galaxy (BCG) as the center for all measurements (see §3.1 for a description of the cluster selection). The $\Delta\Sigma$ is linear in the density and so averaging $\Delta\Sigma$ averages the density directly (again assuming weak shear). Using random points, corrections are applied for contamination of the background source sample with cluster members; a correction that is large but well-determined on small scales, and negligible on large scales. We also correct for residual additive biases in the shear. These result from imperfect correction for biases in the galaxy shapes caused by PSF anisotropy. We use random points for this correction as well, as the additive biases will appear in random points as well as around clusters. This correction is negligible on small scales but significant on large scales.

There are remaining uncertainties in the overall calibration of the mean $\Delta\Sigma$. These come primarily from uncertainties in photometric redshift determinations for the background source galaxies and correction for blurring of the galaxy shapes by the PSF. Simulations of the PSF correction suggest it is good to a few percent under simplified circumstances (Massey et al. 2006). The photometric redshift calibrations are probably less well constrained. Comparisons with LRGs sources, for which the redshift is better determined, suggest the calibrations are good to about 10% (Mandelbaum et al. 2005) and simulations suggest similar numbers (Cunha et al. 2007).

In §9.5 we will present inversions of $\Delta\Sigma$ to the integrated excess mass. These mass profiles are model-independent, but as with the light measurements presented in §2.2, only the excess above the mean can be measured with lensing.

2.2. *Cluster-light Correlations*

We used the method of Masjedi et al. (2006) to estimate the mean number density and luminosity density of galaxies around clusters. This method is essentially a correlation function with units of density: corrections are made for random pairs along the line of sight as well as pairs missed due to edges and holes. We defined two samples: The primary sample denoted p and the secondary sample denoted s. For example, the counts of real data secondaries around real data primaries is denoted D_pD_s, while the counts of real secondaries around random primaries is R_pD_s. In our case, the primaries were galaxy clusters with redshift estimates and the secondaries were the imaging sample with no redshift information.

The mean luminosity density of secondaries around primaries is

$$\bar{\ell}\ w = \frac{D_pD_s}{D_pR_s} - \frac{R_pD_s}{R_pR_s}, \qquad (4)$$

where $\bar{\ell}$ is the mean luminosity density of the secondary sample, averaged over the redshift distribution of the primaries, and w is the projected correlation function. This is the estimator from Masjedi et al. (2006) where the weight of each primary-secondary pair is the luminosity of the secondary. We have written the measurement as $\bar{\ell}w$ to illustrate that the estimator gives the mean density of the secondaries times the projected correlation function w. Only the excess luminosity density with respect to the mean can be measured. Using a weight of unity gives the number density.

The first term in equation 4 estimates the total luminosity density around the clusters including everything from the secondary imaging sample projected along the line of sight, and the second term corrects for the random pairs along the line of sight. Note, the same secondary may be counted around multiple primaries (or random primaries).

The numerator of the first term, D_pD_s, is calculated as:

$$D_pD_s = \frac{\sum_{p,s} L_s}{N_p} = \langle L_{pair}\rangle + \langle L_{pair}^R\rangle = fA\ \bar{\ell}\ (w+1), \qquad (5)$$

where the sum is over all pairs of primaries and secondaries, weighted by the luminosity of the secondary. The secondary luminosity is calculated by K-correcting each secondary galaxy's flux assuming it is at the same redshift as the primary (see §5 for details). The total luminosity is the sum over correlated pairs (L_{pair}) as well as random pairs along the line of sight (L_{pair}^R). By the definition of w, this is the total luminosity per primary times $w+1$. This can be rewritten in terms of the luminosity density of the secondaries $\bar{\ell}$ times the area probed A. Some fraction of the area searched around the lenses is empty of secondary galaxies due to survey edges and holes. The factor f represents the mean fraction of area around each primary actually covered by the secondary catalog. It is a function of pair separation, with a mean

value close to 1 on small scales but then dropping rapidly at large scales.

Again, a single secondary may be counted around multiple primaries and K-corrected to different redshifts. Statistically they will only contribute when paired with a physically associated object due to the background subtraction described below. In fact most of the calculations involved in this measurement are for pairs that are not physically associated, which is part of the reason this is computationally difficult.

The denominator of the first term calculates the factor fA, the actual area probed around the primaries. This term in the denominator corrects for the effects of edges and holes. Also, because it has units of area, we recover the density rather than just the correlation function.

$$D_p R_s = \frac{N^{DR}_{pair}}{\sum_p \left(\frac{d\Omega}{dA}\right)_p \frac{dN}{d\Omega}} = fA. \quad (6)$$

The numerator is the pair counts between primaries and random secondaries, and the denominator is the expected density of pairs averaged over the redshift distribution of the primaries, times the number of primaries. The ratio is the actual mean area used around each primary fA.

The second term in equation 4 accounts for the random pairs along the line of sight. The numerator and denominator are calculated the same way as the first term in equation 4, but with fake primaries distributed randomly over the survey geometry. The redshifts are chosen such that the distribution of redshifts smoothed in bins of $\Delta z = 0.01$ match that of the clusters.

$$R_p D_s = \frac{\sum_{pr,s} L_s}{N_p} = \langle L^R_{pair} \rangle = f^R A^R \, \bar{\ell} \quad (7)$$

$$R_p R_s = \frac{N^{RR}_{pair}}{\sum_{pr} \left(\frac{d\Omega}{dA}\right)_{pr} \frac{dN}{d\Omega}} = f^R A^R. \quad (8)$$

The ratio of these two terms, $R_p D_s / R_p R_s$, calculates the mean density of the secondaries after correcting for the survey geometry.

By replacing the luminosity of the secondaries with a weight of unity we recover the mean density of pairs, rather than their number density. The ratio of these two measurements gives the mean luminosity per secondary.

The density measured with this technique could be tabulated in various ways, typically as a function of projected radial separation R. We tabulate in a cube which represents bins of separation R, luminosity L, and color $g-r$. This facilitates the study of the radial dependence of the luminosity function and the color-density relation.

These profiles can be inverted to the three-dimensional excess density and integrated to get the total excess light. We will present this formalism in section 9.4.

3. DATA

The data used for lensing was described in detail in paper I (Sheldon et al. 2007) and the cluster sample is described in Koester et al. (2007a,b) with the modifications detailed in Sheldon et al. (2007). We will briefly describe relevant details of the cluster sample and give a full description of the galaxies used as light tracers in the cluster-light cross-correlation measurements. All the primary data in this study come from the Sloan Digital Sky Survey (SDSS; York et al. 2000) data release 4 (Adelman-McCarthy et al. 2006).

3.1. *Cluster Sample*

Full details of the cluster finder and catalog can be found in Koester et al. (2007a,b). The cluster finder is a red-sequence method, limited to the redshift range 0.1-0.3. The basic galaxy count N_{200} is the number of galaxies on the red sequence with rest-frame i-band luminosity $L > 0.4L_*$ within r^{gals}_{200}. The i-band L_* used in the cluster finder is the $z = 0.1$ value from Blanton et al. (2003b), corresponding to $M_* - 5\log_{10}h = -20.82 \pm 0.02$. The radius r^{gals}_{200} is determined from the size-richness relation presented in Hansen et al. (2005). Note, this relation gives roughly a factor of 2 larger radius than the r^{mass}_{200} determined from the mass in Paper II (Johnston et al. 2007b). The published catalog contains clusters with $N_{200} \geq 10$, and we augment this catalog with $N_{200} \geq 3$ objects. The cluster photometric redshifts are accurate to 0.004 over our redshift range with a scatter of $\Delta z \sim 0.01$ for $N_{200} \geq 10$; the scatter degrades to $\Delta z \sim 0.02$ for $N_{200} \geq 3$, with the same accuracy.

3.2. *Galaxy Sample*

For the cluster-light cross-correlations we separated galaxies from stars using the Bayesian techniques developed in Scranton et al. (2002). The primary source of confusion in star-galaxy separation at faint magnitudes is shot noise. Stars scatter out of the stellar locus and galaxies scatter into the stellar locus. This technique uses knowledge of the true size distribution of stars and galaxies as a function of apparent magnitude to assign each object a probability of being a galaxy.

We characterized the distribution of star and galaxy sizes as a function of magnitude and seeing using the deeper southern SDSS stripe. The SDSS southern stripe has a been repeatedly scanned. We chose regions of sky which were scanned at least 20 times and chose the 20 best-seeing observations for each object. We then simply added the flux at the catalog level to increase the S/N. Thus, the selection is close to that of single scans but with a better measurement; S/N at a given magnitude is higher, and the distribution of measured sizes is closer to the truth. For a range of seeing values, we then calculated the probability that an object in a single-epoch image with a given magnitude and size is truly a galaxy, and applied this to all objects in the survey. The resulting distribution is highly peaked at probability 0 and 1, such that our chosen probability cut at $p > 0.8$ results in a sample $\gtrsim$99% pure within our magnitude limit.

We chose a volume and magnitude limited galaxy sample for $L_{0.25i} > 10^{9.5} h^{-2} L_\odot$ (or $M_{0.25i} - 5\log_{10} h <$-19.08). and $z < 0.3$. This corresponds to an apparent magnitude limit of $i < 21.3$, and color limits of $g-r < 2$ and $r-i < 1$. All magnitudes are SDSS model magnitudes.

4. SURVEY GEOMETRY

We characterized the survey geometry using the SDSSPix code [13]. This code represents the survey using nearly equal area pixels, including edges and holes from missing fields and "bad" areas near bright stars. We removed areas with extinction greater than 0.2 magnitudes in the dust maps of Schlegel et al. (1998). This window function was used in the cluster finding and in defining

[13] http://lahmu.phyast.pitt.edu/∼scranton/SDSSPix/

the galaxy catalog for the cross correlations. By including objects only from within the window, and generating random catalogs in the same regions, we controlled and corrected for edges and holes in the observed counts as described in §2.

5. K-CORRECTIONS

We calculated K-corrections using the template code `kcorrect` from Blanton et al. (2003a). This code is accurate but too slow to calculate the K-corrections for the billions of pairs found in the cross-correlations. To save time we computed the K-correction on a grid of colors in advance. We took galaxies from the SDSS Main sample as representative of all galaxy types. We then computed their K-corrections on a grid of redshifts between 0 and 0.3, the largest redshift considered for clusters in this study. The mean K-correction in a $21 \times 21 \times 80$ grid of observed $g-r, r-i$, and z was saved. We interpolated this cube when calculating the K-correction for each neighboring galaxy. This interpolation makes the calculation computationally feasible for this study, but is still the bottleneck.

We chose to K-correct to band-passes shifted to the mean cluster redshift 0.25 rather than redshift 0 to minimize the corrections. We will refer to all such magnitudes with a superscript, e.g. ${}^{0.25}i$. For a full discussion of the band-shifting process see Blanton et al. (2003a).

6. CLUSTER GALAXY POPULATION MEASUREMENTS

6.1. *Radial, Color and Luminosity Binning*

Using the estimator presented in §2.2, we measured the number and luminosity density of galaxies around the clusters as a function of radius from the BCG, color, and luminosity. We counted pairs with radius $0.02 < R < 11.5h^{-1}$ Mpc, $0 < {}^{0.25}(g-r) < 2$ and $9.5 < \log_{10}(L_{0.25i}/L_\odot) < 11.7$. This cube has 18 bins in radius, and 20 bins in color and luminosity. The initial cube before background correction was kept separately for each cluster to allow flexibility when later estimating the average profile. Two versions of this cube were kept, one with number counts and another with the total luminosity. In other words, in the first case we counted each galaxy and in the other we counted the luminosity. Another set of measurements was also performed to $30h^{-1}$ Mpc, but binning only in radial separation to save resources. More detailed analysis of the full cube will presented in Hansen et al. (2007); here we will present what is needed for the particulars of the M/L measurement.

6.2. *Random Catalogs*

We generated random catalogs uniformly over the survey area using the window function described in §4. We chose the redshift distribution to be that of constant density in comoving volumes over the redshift range of the clusters. We matched subsets of these redshifts to the redshift distribution of each cluster subsample as described in §6.3.

We performed the same galaxy counting as described in §6.1 for a set of 15 million random points in order to correct for the random background. These are used in the RD term from the estimator described in §2. We also ran sets of 15 million random points for the DR and RR terms.

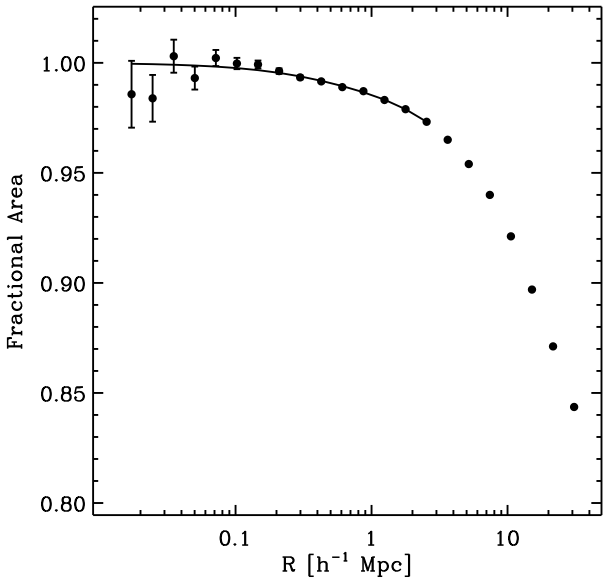

FIG. 1.— Mean fractional area searched relative to the total area in each radial bin for the 8th cluster richness sample ($12 \leq N_{200} \leq 17$). Edges and holes dilute the true galaxy counts, biasing the measured density. This effect is negligible on small scales, but becomes important for large separations when a higher fraction of clusters are closer to the edge than the search radius. Due to small area at small separations, the value is not well determined, but must approach unity smoothly. We model this with a polynomial constrained to be unity on small scales, shown as the solid curve. For larger scales no model is needed.

6.3. *Histogram Matching*

The redshifts used for random points must statistically match that of each cluster sample in order for the background subtraction to be accurate. The random primaries described in §6.2 were generated with constant comoving density. We drew random redshifts from this sample such that the distribution matched that of the cluster sample when binned with $\Delta z = 0.01$.

6.4. *Cluster Richness Binning*

Because the measurements before background correction were saved for each cluster separately, the clusters could be binned at a later time to produce mean density profiles. For this work we binned into 12 bins of N_{200} and 16 bins of i-band cluster luminosity L_{200}, where the luminosity is that of the N_{200} red galaxies counted within r_{200}^{gals} as described in §3.1. These bins were chosen to correspond with the binning presented in the lensing analysis of Sheldon et al. (2007). Some statistics of this sample are shown in Tables 1 and 2.

6.5. *Corrections for Edges and Holes*

The terms D_pR_s and R_pR_s introduced in §2.2 correct for the survey edges and holes by measuring the actual area searched. An example DR is shown in Figure 1, generated for one of the richness bins described in §6.4. This is expressed as the mean fractional area searched relative to the area in the bin. For small separations, edges and holes make little difference so the fractional area is close to unity. On larger scales edges are important.

On small scales the number of pairs in each bin is relatively small so the correction is not as well constrained.

TABLE 1
$\Delta M/\Delta L$ Statistics for N_{200} Bins

$\langle N_{200}\rangle$	ΔL^{tot}_{200}	ΔM_{200}	$\left(\frac{\Delta M}{\Delta L}\right)_{200}$	$\left(\frac{\Delta M}{\Delta L}\right)_{rmax}$	$\langle L^{gal}_{10}\rangle$	$r_{1/2}$	α	$\left(\frac{\Delta M}{\Delta L}\right)_{asym}$
3	3.84 ± 0.02	3.99 ± 0.16	101 ± 10	275 ± 313	0.98 ± 0.10	0.25 ± 0.07	1.34 ± 0.11	226 ± 33
4	4.86 ± 0.04	5.78 ± 0.26	108 ± 14	347 ± 229	1.02 ± 0.10	0.44 ± 0.15	1.05 ± 0.08	306 ± 42
4	5.98 ± 0.07	8.84 ± 0.44	166 ± 18	455 ± 234	1.02 ± 0.11	0.47 ± 0.16	1.06 ± 0.08	357 ± 44
5	7.22 ± 0.09	12.88 ± 0.64	170 ± 22	341 ± 183	0.93 ± 0.12	0.24 ± 0.05	1.46 ± 0.13	285 ± 28
7	7.99 ± 0.12	12.54 ± 0.78	122 ± 27	540 ± 231	1.10 ± 0.11	0.30 ± 0.31	1.02 ± 0.14	271 ± 59
8	9.16 ± 0.15	16.58 ± 1.20	179 ± 30	353 ± 157	1.10 ± 0.11	0.44 ± 0.12	1.16 ± 0.11	378 ± 41
9	11.51 ± 0.14	26.88 ± 1.03	229 ± 22	354 ± 140	1.04 ± 0.10	0.30 ± 0.05	1.27 ± 0.09	342 ± 24
13	16.23 ± 0.22	42.67 ± 1.39	257 ± 21	327 ± 133	1.08 ± 0.09	0.28 ± 0.05	1.12 ± 0.08	355 ± 24
20	23.74 ± 0.38	70.18 ± 2.54	319 ± 27	321 ± 145	1.24 ± 0.11	0.19 ± 0.03	1.37 ± 0.11	349 ± 21
31	36.88 ± 0.80	131.66 ± 5.02	333 ± 32	300 ± 175	1.27 ± 0.13	0.20 ± 0.04	1.35 ± 0.16	394 ± 26
50	53.82 ± 1.95	203.71 ± 9.57	379 ± 43	525 ± 307	0.94 ± 0.24	0.15 ± 0.02	2.19 ± 0.29	404 ± 21
92	104.33 ± 5.16	516.19 ± 38.78	489 ± 75	547 ± 332	0.93 ± 0.53	0.11 ± 0.01	3.91 ± 0.65	485 ± 33

Note. — $(\Delta M/\Delta L)_{22\mathrm{Mpc}}$ is the mass-to-light ratioi within $22h^{-1}$Mpc. The $\Delta M/\Delta L_{asym}$ is the result of fitting a model. The model is not a physical model, so these uncertainties should be considered lower limits. No attempt was made to account for mis-centering of the BCGs relative to the halo mass peak; this affects the ΔM_{200} but should have little effect on $(\Delta M/\Delta L)_{200}$, and no effect on $(\Delta M/\Delta L)_{22\mathrm{Mpc}}$. Masses are in units of $h^{-1}M_\odot$, luminosities are measured in units of $h^{-2}10^{10}L_\odot$ and mass-to-light ratios in units of $hM_\odot/L_\odot$. $r_{1/2}$ is in units of h^{-1}Mpc.

However, we know that the fractional area must approach unity smoothly, and this can be seen from visual inspection. To smooth the result, we fit a fifth order polynomial, constrained to be unity on small scales, to the fractional area as a function of the logarithmic separation. Due to the weighting, this results in a curve that approaches unity smoothly on small scales, yet matches intermediate separation points exactly. Points on larger scales are well-constrained and do not need smoothing.

7. LUMINOSITY DENSITY AT Z=0.25

We are interested in the background luminosity density at z=0.25, in the $^{0.25}i$ band, for comparisons with our luminosity measurements. We use an evolved version of the SDSS spectroscopic sample (whose median redshift is about $z \sim 0.1$). For this purpose, we use the DR4 version of the New York University Value-Added Galaxy Catalog (NYU-VAGC; Blanton et al. 2005). We select a subset of the galaxies in the redshift range $0.01 < z < 0.25$, in the apparent magnitude range $14.5 < m_r < 17.6$. The NYU-VAGC provides the angular completeness map necessary to calculate for each galaxy the quantity $V_{\max}$, the maximum volume over which we can observe it. We do so using the same method as used by Blanton (2006), which accounts for the evolution and K-corrections within this redshift range. We use the `kcorrect` v4_1_4 code of Blanton & Roweis (2007) to estimate the $^{0.25}i$ band, Galactic extinction-corrected, K-corrected absolute magnitude of each galaxy, based on the model fluxes provided by SDSS.

Finally, we evolution-correct these magnitudes in the following way, based on the results of Blanton (2006). For each galaxy we apply a simple correction of the form:

$$M_{0.25_i}(z = 0.25) = M_{0.25_i}(z) + A(z - 0.25) \qquad (9)$$

For galaxies on the blue sequence, based on their $^{0.25}(g-r)$ colors, we use $A = 0.65$. For galaxies on the red sequence we use $A = 0.35$. These values are calculated by evaluating the simple star-formation history models of Blanton (2006). These models explain the evolution of the blue and red sequences in the $^{0.1}g$ band well, and we use the corresponding predictions for the $^{0.25}i$ band. In practice, these corrections are quite small (at most 0.16 mag), and so the inevitably uncertainty in this correction is likely to be unimportant.

By using the evolution-corrected magnitudes and weighting each galaxy by $1/V_{\max}$, we estimate the luminosity function using the method of Schmidt (1968). The resulting luminosity density for galaxies above our luminosity threshold $10^{9.5}h^{-2}L_\odot$ is $(1.61 \pm 0.05) \times 10^8 h$ $L_\odot\mathrm{Mpc}^{-3}$ in comoving coordinates, or $(3.14 \pm 0.10) \times 10^8$ h $L_\odot\mathrm{Mpc}^{-3}$ in physical coordinates. Our luminosity limit is equivalent to $M_{0.25_i} - 5\log_{10} h <$ -19.08, where we use $M_\odot = 4.67$ in the $^{0.25}i$ band. The uncertainty is dominated by the absolute calibration of the SDSS. Fitting a single Schechter function to the luminosity function, we find that $M_* - 5\log_{10} h \approx -20.9$ (with $\alpha \approx -1.21$), equivalent to $L_* = 1.7 \times 10^{10}h^{-2}L_\odot$. Thus the lower luminosity threshold corresponds to $0.19L_*$.

8. SIMULATIONS

In order to study the impact of the MaxBCG algorithm on our conclusions, and in particular the differences between how our method operates on dark matter halos and on MaxBCG clusters, we have repeated the luminosity measurements on a mock catalog. These catalogs, which have been used in previous maxBCG studies (Rozo et al. 2007b,a; Koester et al. 2007a; Johnston et al. 2007b), populate a dark matter simulation with galaxies using the ADDGALS technique Wechsler et al. (2008). This method is designed to populate large volume simulations with galaxy populations that have realistic luminositys, colors, clustering properties, and cluster populations.

The catalog is based on the light-cone from the Hubble Volume simulation (Evrard et al. 2002), and extends from $0 < z < 0.34$. Galaxies are assigned directly to dark matter particles in the simulation, with a luminosity-dependent bias scheme that is tuned to match local clustering data. The galaxy luminosities are first assigned in the $^{0.1}r$-band, drawn from the luminosity function of Blanton et al. (2003b). The luminosity function is assumed to evolve with Q=1.3 magnitudes per unit redshift. We first constrain the relationship between galaxy luminosity and Lagrangian matter densities on a scale of $\sim M*$, using the luminosity-dependent two-point clustering of SDSS galaxies (Zehavi et al. 2005). For each galaxy, a dark matter particle is then chosen on the ba-

TABLE 2
$\Delta M/\Delta L$ Statistics for L_{200} Bins

$\langle L_{200}\rangle$	ΔL^{tot}_{200}	ΔM_{200}	$\left(\frac{\Delta M}{\Delta L}\right)_{200}$	$\left(\frac{\Delta M}{\Delta L}\right)_{rmax}$	$\langle L^{gal}_{10}\rangle$	$r_{1/2}$	α	$\left(\frac{\Delta M}{\Delta L}\right)_{asym}$
5.6	3.75 ± 0.04	4.51 ± 0.30	114 ± 20	363 ± 263	1.04 ± 0.11	0.70 ± 0.50	0.94 ± 0.08	465 ± 96
7.0	4.63 ± 0.04	5.32 ± 0.32	113 ± 18	260 ± 238	1.03 ± 0.11	0.39 ± 0.19	1.15 ± 0.11	300 ± 56
8.7	5.98 ± 0.06	7.64 ± 0.40	116 ± 18	458 ± 213	1.01 ± 0.11	0.18 ± 0.05	1.44 ± 0.15	200 ± 25
10.8	7.62 ± 0.07	11.80 ± 0.53	169 ± 18	283 ± 146	1.11 ± 0.12	0.42 ± 0.12	1.09 ± 0.08	315 ± 36
13.5	9.48 ± 0.10	15.68 ± 0.70	129 ± 19	405 ± 187	1.05 ± 0.11	0.52 ± 0.13	1.06 ± 0.06	357 ± 38
16.9	11.82 ± 0.13	23.68 ± 0.94	193 ± 19	374 ± 173	1.11 ± 0.11	0.52 ± 0.15	0.98 ± 0.07	399 ± 42
21.1	14.12 ± 0.19	29.34 ± 1.26	214 ± 23	526 ± 184	1.16 ± 0.11	0.33 ± 0.12	1.08 ± 0.10	319 ± 36
26.3	17.77 ± 0.27	41.87 ± 1.76	215 ± 25	332 ± 137	1.15 ± 0.11	0.33 ± 0.09	1.13 ± 0.10	357 ± 35
32.9	21.75 ± 0.35	54.22 ± 2.46	265 ± 27	408 ± 223	1.02 ± 0.12	0.21 ± 0.05	1.33 ± 0.13	329 ± 28
40.9	26.39 ± 0.56	72.34 ± 3.31	279 ± 32	315 ± 159	1.30 ± 0.15	0.22 ± 0.05	1.28 ± 0.13	343 ± 27
51.2	33.96 ± 0.84	105.56 ± 5.22	284 ± 39	237 ± 218	1.24 ± 0.16	0.24 ± 0.09	1.15 ± 0.15	368 ± 41
64.1	45.66 ± 1.23	162.02 ± 8.44	354 ± 42	225 ± 224	1.20 ± 0.21	0.32 ± 0.14	1.17 ± 0.15	451 ± 56
79.9	51.09 ± 1.94	172.42 ± 10.72	339 ± 52	347 ± 301	1.28 ± 0.46	0.18 ± 0.03	1.65 ± 0.25	366 ± 29
98.7	56.53 ± 3.12	194.84 ± 15.52	291 ± 74	384 ± 286	1.11 ± 0.64	0.12 ± 0.04	2.53 ± 0.63	321 ± 29
124.6	81.86 ± 5.88	266.15 ± 23.66	370 ± 70	-286 ± 474	1.12 ± 0.67	0.15 ± 0.03	5.67 ± 2.66	324 ± 38
184.7	123.86 ± 9.07	593.94 ± 44.55	476 ± 72	626 ± 327	0.79 ± 0.54	0.24 ± 0.05	1.49 ± 0.16	456 ± 40

Note. — Same as table 1 for clusters binned by L_{200}.

sis of this density with some $P(\delta|M_r)$. Each mock galaxy is then assigned to a real SDSS galaxy that has approximately the same luminosity and local galaxy density, measured here as the distance to the 5th nearest neighbor. The color for each mock is then given by the SED of this matched galaxy transformed to the appropriate redshift. This procedure produces a catalog which matches several statistics of the observed SDSS population, including the location, width and evolution of the ridgeline, which makes it ideal for testing the maxBCG algorithm. The luminosity limit for galaxies in these mocks is slightly lower that of the cluster finder $L > 0.4L_*$, so the catalogs are well-designed for testing the MaxBCG algorithm. However, this limit is higher than for our measurements, so the results cannot compared at low luminosities. In this paper, we use the simulations just to understand the effects of cluster selection on our measurements, and focus on high luminosities (see §9.2).

9. RESULTS

In the following sections we show the results for clusters binned by N_{200}. Similar results were obtained binning by L_{200}, and we summarize all results in Tables 1 and 2, but for the sake of brevity we include plots only for the N_{200} binning.

9.1. *The Radial Dependence of the Joint Luminosity-color function*

Figure 2 shows the joint color-luminosity distribution function for each radial bin in the 8th cluster richness sample ($12 \leq N_{200} \leq 17$). Similar distributions were created for each of the cluster richness bins used in this study. We will present detailed analyses of these type of data in Hansen et al. (2007), but we also present a sample here in order to demonstrate a few aspects important for the M/L study.

The first point is that the population is quite different at small scales relative to large scales. On small scales, near the BCGs, the galaxy population is dominated by red galaxies, while on large scales the color distribution looks more like the cosmological average. Similarly, on large scales the luminosity function looks more like that of the average, although they are poor fits to Schechter functions. These facts are relevant to the M/L for a few reasons. We want to make sure that the population we are seeing around clusters makes sense; that we, for example, are complete in the color-luminosity range we have probed. Again, detailed analysis will come in Hansen et al. (2007), but these color and luminosity trends are exactly what is expected. We will discuss the shape of the luminosity function in §9.2.

9.2. *The Radial Dependence of the Luminosity function*

Projecting the two-dimensional color-luminosity plots from Figure 2 across the color axis produces the luminosity function in each radial bin. Recall that to produce these curves we have statistically subtracted the background, so the luminosity function is that minus the mean density of the universe. The value of these functions in a luminosity bin i is

$$\phi_{c,i}(R) = n(R)_i - \bar{n_i} = \phi_i w_{c,i}(R), \qquad (10)$$

where $w_{c,i}(R)$ is the projected cross-correlation function between clusters and galaxies in luminosity bin i at projected radius R and ϕ_i is the value of the luminosity function of the universe in that luminosity bin i.

Because of the statistical subtraction, the value of the luminosity function in luminosity bin i is weighted by the cross-correlation function of clusters with galaxies of that luminosity. This is important because galaxies of different luminosities correlate with clusters differently. An extreme example of this is demonstrated for the lowest L_{200} bin in Figure 3, which shows $\phi_{c,i}$ in each radial bin. This Figure shows that, near the virial radius, the inferred luminosity function for small groups is actually negative for galaxies with $L_{0.25_i} \sim 10^{10.7} L/L_\odot$. This is not because there is a negative number density of these galaxies around the groups, but because they are anti-correlated with the groups at this separation. This means that, near the virial radius, there are fewer of these high luminosity galaxies relative to the background.

This effect is strongest in our lowest N_{200} bin, although there is a slight feature in the luminosity function at virial radius for high luminosity galaxies the first few cluster bins.

In order to understand whether these effects are physical, due to selection effects of the cluster finder, or are artifacts of our method, we ran the MaxBCG algorithm

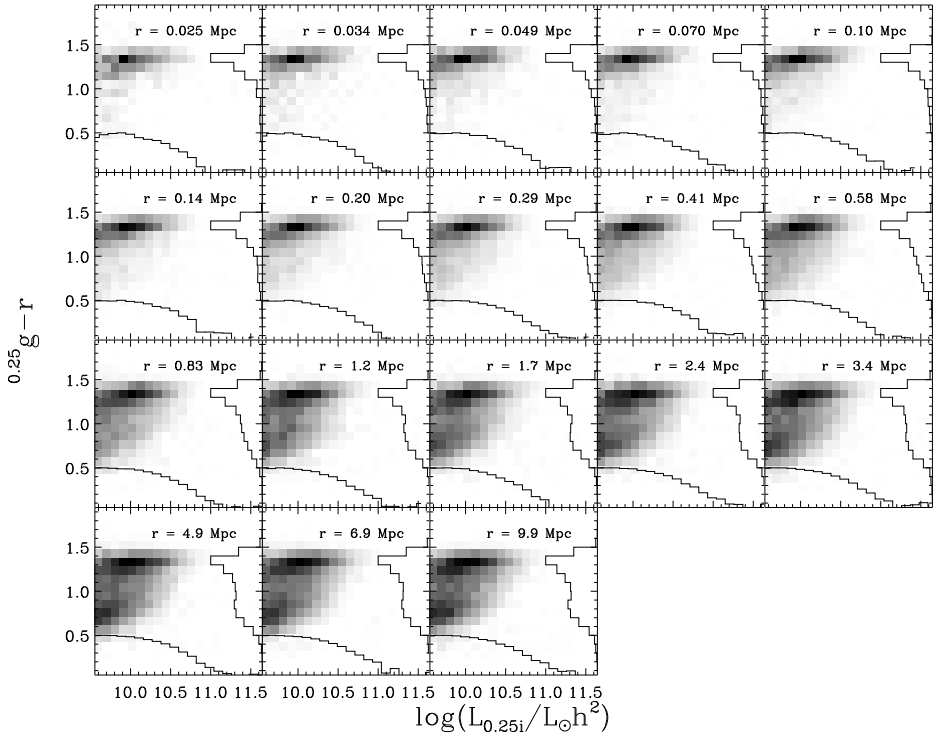

FIG. 2.— Joint galaxy $^{0.25}(g-r)$ and $^{0.25}i$-band luminosity densities as a function of projected separation from BCGs for the 8th cluster richness bin ($12 \leq N_{200} \leq 17$). The fluxes are expressed in the z=0.25 shifted bandpass. Each frame corresponds to a different radial bin; the radius is indicated in the legend. The one dimensional distributions for color and luminosity are also shown. The luminosity distribution is expressed as log of the number density as a function of log luminosity; the color distribution is linear density as a function of color. At small separations red galaxies dominate while on large scales there is a bivariate color distribution similar to the cosmological average. A smaller fraction of galaxies is highly luminous at small separations as compared to large.

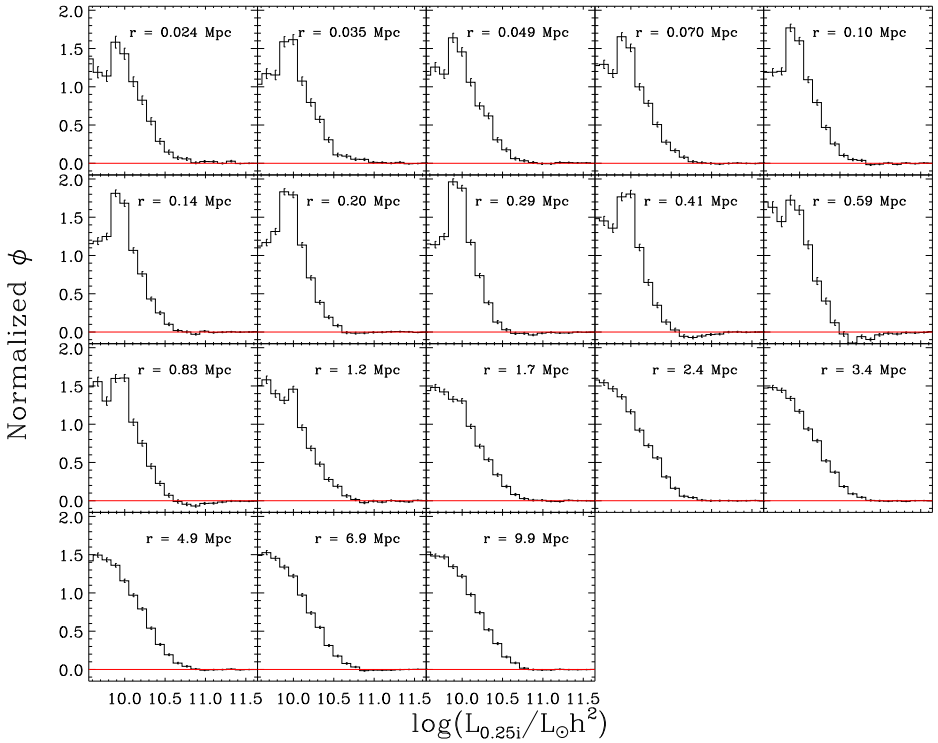

FIG. 3.— Excess luminosity functions for the first cluster richness bin. This is the integral across the color axis of the joint densities such as those shown for another richness bin in Figure 2. As in that Figure, each panel is a radial bin with mean radius indicated in the legend. Each bin in the excess luminosity function is the amplitude of the projected cluster-galaxy cross-correlation function at that radial separation times the mean density. In some bins the galaxies are anti-correlated. This cluster richness bin was chosen as the extreme examples of these anti-correlations; they are smaller or non-existent in higher richness bins. As discussed in §9.2, this feature is a result of the MaxBCG selection function at low richness.

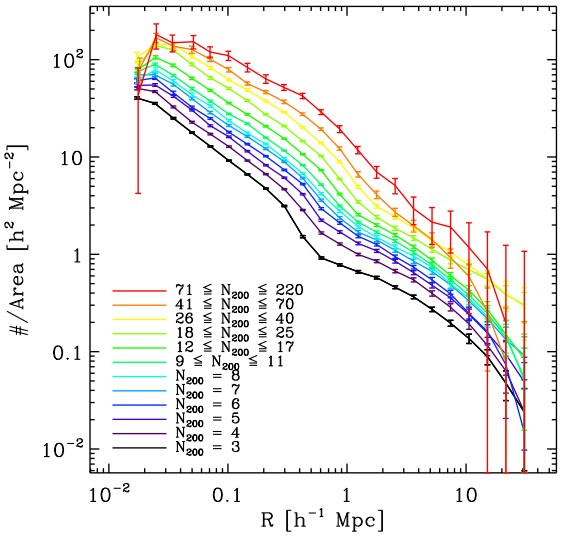

FIG. 4.— Excess radial number density for each of the cluster N_{200} bins. These curves are the integral of the excess luminosity functions as shown in Figure 3.

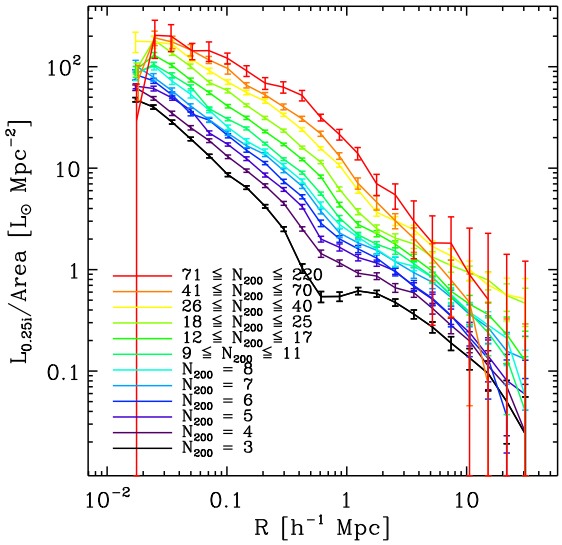

FIG. 5.— Excess radial $^{0.25}i$-band luminosity density for each of the cluster N_{200} bins. These curves are the integral of luminosity-weighted luminosity functions.

and our cross-correlation code on the simulation-based mock catalogs described in §8. We performed this test twice, stacking on both cluster centers (BCGs) and halo centers. For the mock stacked on maxBCG clusters, a similar effect is seen, although it is suppressed relative to the effect in the real data. As in the data, the effect is strongest in the lowest richness bin. When the measurement is done around halo centers, there is no significant effect seen. This indicates that it is mostly an effect introduced by the selection criteria of the MaxBCG algorithm.

This lowest luminosity bin is peculiar in that it requires the close proximity of only three very luminous red galaxies, one of which has extreme BCG-like luminosity. This an unusual situation; BCGs of this luminosity are usually surrounded by many more galaxies. In order to find only two such galaxies within a few hundred kpc of a BCG type galaxy, the algorithm selects objects embedded in slight under-densities. This can occur naturally in the MaxBCG algorithm due to the percolation step, which does not allow clusters to be embedded within larger clusters. This may limit low richness systems to very particular regions of space.

9.3. *Radial Luminosity and Number Density*

Further integrating the luminosity functions from section 9.2 across the luminosity axis results in the excess number density of galaxies. We also have luminosity functions weighted by luminosity (we count luminosity instead of 1 for each galaxy) and this gives the excess luminosity density above the mean. These are shown in Figures 4 and 5 respectively. Each curve represents the excess density for each of the cluster L_{200} bins.

Again, it is important to remember that these curves are background subtracted, and are thus the number and luminosity densities above the mean. These terms can be written in terms of correlation functions:

$$n(R) - \bar{n} = \bar{n}\; w_{c,g}(R) \tag{11}$$

$$\ell(R) - \bar{\ell} = \bar{\ell}\; w_{c,\ell}(R) \tag{12}$$

where $\bar{n}$ and $\bar{\ell}$ are the mean number and luminosity density of galaxies over the explored luminosity range, and $w_{c,g}(R)$ and $w_{c,\ell}(R)$ are the projected cluster-galaxy and cluster-luminosity cross-correlation functions, averaged over all galaxies in the luminosity range at projected radius R, weighted by the luminosity function.

It is tempting to interpret the ratio of the excess luminosity to excess number densities as the mean luminosity as a function of radius. Given that there can be negative densities with respect to the mean at some luminosities when there are anti-correlations, as shown in Figure 3, this is not always the correct interpretation.

9.4. *Integrated Luminosity Profiles*

We will use integrated luminosity profiles to compute the mean M/L within a given three-dimensional radius r. We invert the projected two-dimensional profile shown in Figure 5 using a standard Abel type inversion (e.g Plummer 1911):

$$\Delta\ell(r) = \ell(r) - \bar{\ell} = \frac{1}{\pi}\int_r^\infty \mathrm{d}R \frac{-\ell'(R)}{\sqrt{r^2 - R^2}}, \tag{13}$$

where we have re-used the notation for the excess luminosity density from equation 11 but replaced projected radius R with three-dimensional radius r. We have been explicit here in indicating we measure the density minus the mean $\ell(r) - \bar{\ell}$. Thus the $\Delta\ell(r)$ is proportional to the cluster-light cross-correlation function:

$$\Delta\ell(r) = \bar{\ell}\; \xi_{c\ell}(r) \tag{14}$$

The assumption behind the inversion in equation 13 is that $\ell(R)$ is the line of sight projection of a spherically symmetric three-dimensional function $\ell(r)$. This follows from the isotropy of the universe as long as the cluster selection function does not select structures preferentially aligned relative to us.

Because the maximum separation we measure is $30h^{-1}$ Mpc rather than infinity, we cannot accurately calculate $\Delta\ell(r)$ over the entire range. We lose the last point entirely, and the second to last point, at $22h^{-1}$Mpc, must

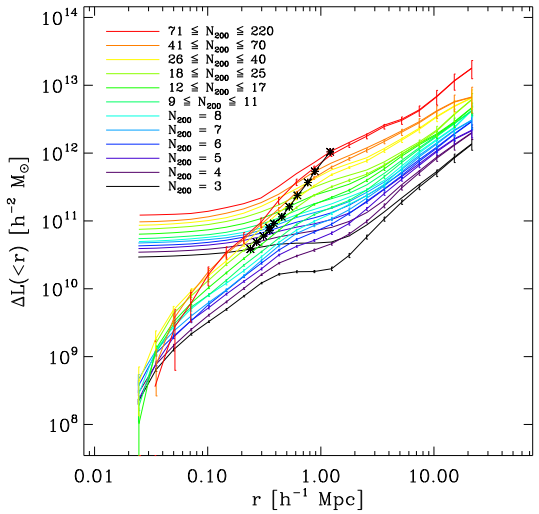

FIG. 6.— Excess 3D $^{0.25}i$-band luminosity profiles for each of the cluster N_{200} bins. The 2D profiles from Figure 5 were de-projected and integrated over radius. The curves without error bars include the BCG luminosity, those with errors do not. The mean r_{200}^{mass}, determined from the mass profiles in §9.5, is marked for each curve.

be corrected slightly for the endpoint. We perform a power-law extrapolation of the profile and find this to be a 5% upward correction.

We then integrate the excess luminosity density to obtain the total luminosity within radius r. Because the profile only extends to $25h^{-1}$kpc, we are missing some light interior to this radius. This light is dominated by the BCG however, so we can add that component back in as the average BCG luminosity for a given cluster sample:

$$\Delta L(<r) = \langle L_{BCG} \rangle + \int_{rmin}^{r} \mathrm{d}r 4\pi r^2 \Delta\ell(r), \qquad (15)$$

where we have again been explicit in defining our measured quantity as $\Delta L(<r)$, the integrated excess luminosity above the mean density.

Figure 6 shows this quantity $\Delta L(<r)$ for the richness and luminosity cluster binning. There are two curves for each richness bin: one including the mean BCG luminosity $\langle L_{BCG} \rangle$ and one without. The light is dominated by the BCG on small scales. The luminosity within r_{200}^{mass} is marked with an asterisk. The r_{200}^{mass} is calculated from the mass profiles (see §9.5).

9.5. *Integrated Mass Profiles*

The cluster mass profiles were measured from the lensing measurements presented in Sheldon et al. (2007) and Johnston et al. (2007b). These measurements were performed for the same samples presented above. The basic lensing measurement is $\Delta\Sigma$, which is a projected quantity:

$$\Delta\Sigma \equiv \bar{\Sigma}(<R) - \bar{\Sigma}(R) \ , \qquad (16)$$

where $\bar{\Sigma}$ is the projected surface mass density at radius R and $\bar{\Sigma}(<R)$ is the mean projected density within radius R. The subtraction in this equation is a manifestation of the mass sheet degeneracy.

In Johnston et al. (2007b) we inverted the projected profiles to the three-dimensional excess mass density using the techniques presented in Johnston et al. (2007a). This inversion is a procedure analogous to the inversion of the luminosity density presented in §9.4:

$$-\frac{\mathrm{d}\Sigma}{\mathrm{d}R} = \frac{\mathrm{d}\Delta\Sigma}{\mathrm{d}R} + 2\frac{\Delta\Sigma}{R}$$
$$\Delta\rho(r) \equiv \rho(r) - \bar{\rho} = \frac{1}{\pi}\int_r^\infty \mathrm{d}R \frac{-d\Sigma/\mathrm{d}R}{\sqrt{R^2 - r^2}}. \qquad (17)$$

Again, the assumption is that the profiles are projections of spherically symmetric three-dimensional functions. We can recover the total excess mass within radius r, including that within our innermost radius, because $\Delta\Sigma$ is itself a non-local measurement:

$$\Delta M(<r) = \pi R^2 \Delta\Sigma(R) +$$
$$2\pi \int_R^\infty \mathrm{d}r \ r\Delta\rho(r) \left[\frac{R^2}{\sqrt{r^2 - R^2}} - 2\left(r - \sqrt{r^2 - R^2}\right)\right] \qquad (18)$$

As with the luminosity inversions, the last point must be thrown out and a 5% correction is applied to the second to last point. Figure 7 shows these excess mass profiles for the N_{200} binnings. These data are the same as presented in Johnston et al. (2007b).

In order to get a size scale for each cluster sample, we fit a simple model to the data. The model is that of an NFW profile on small scales (Navarro et al. 1997) and linear correlations on large scales. This model was presented in detail in Johnston et al. (2007b). For this paper, we only use this fit in order to estimate a size r_{200}^{mass}, from which we can also calculate the mass ΔM_{200}. The r_{200}^{mass} is the radius where the mean mass density falls to 200 times the critical density, and M_{200} is the mass contained within that radius. This radius r_{200}^{mass} will be a reference point for the M/L measurements. The fits for each richness bin are shown in Figure 7 and r_{200}^{mass} is marked for reference. Note, these values are somewhat different than those in Johnston et al. (2007b) where power-law interpolation was used to extract r_{200}^{mass}.

In Johnston et al. (2007b) it is shown that if a fair fraction of the BCGs are mis-centered relative to the halo center (or peak) the profile can be strongly effected. In that work a mis-centering distribution was determined from simulations, and used to recover the underlying halo mass distribution. In this work we do not try to recover halo masses, but work directly with the observations around the BCGs chosen as centers. Thus it is important to keep in mind that these are the mass profiles (and light profiles) around BCGs, not necessarily peaks of the halo mass distribution. This is probably not a large effect for the M/L at the virial radius, and is negligible on the largest scales. On the other hand, for relatively small radii the shape of the M/L profile around BCGs may be different than that around halo centers.

9.6. *Mass-to-light Ratio Profiles*

In order to generate $\Delta M/\Delta L$ profiles we simply divide the integrated excess mass ΔM by the integrated excess light ΔL profiles. These profiles are shown for each cluster richness bin in Figure 8.

The $\Delta M/\Delta L$ is shown with and without the mean BCG luminosity. When the mean BCG luminosity is included the profile rises steeply and then flattens out at large radius. The r_{200}^{mass} is marked for reference. The

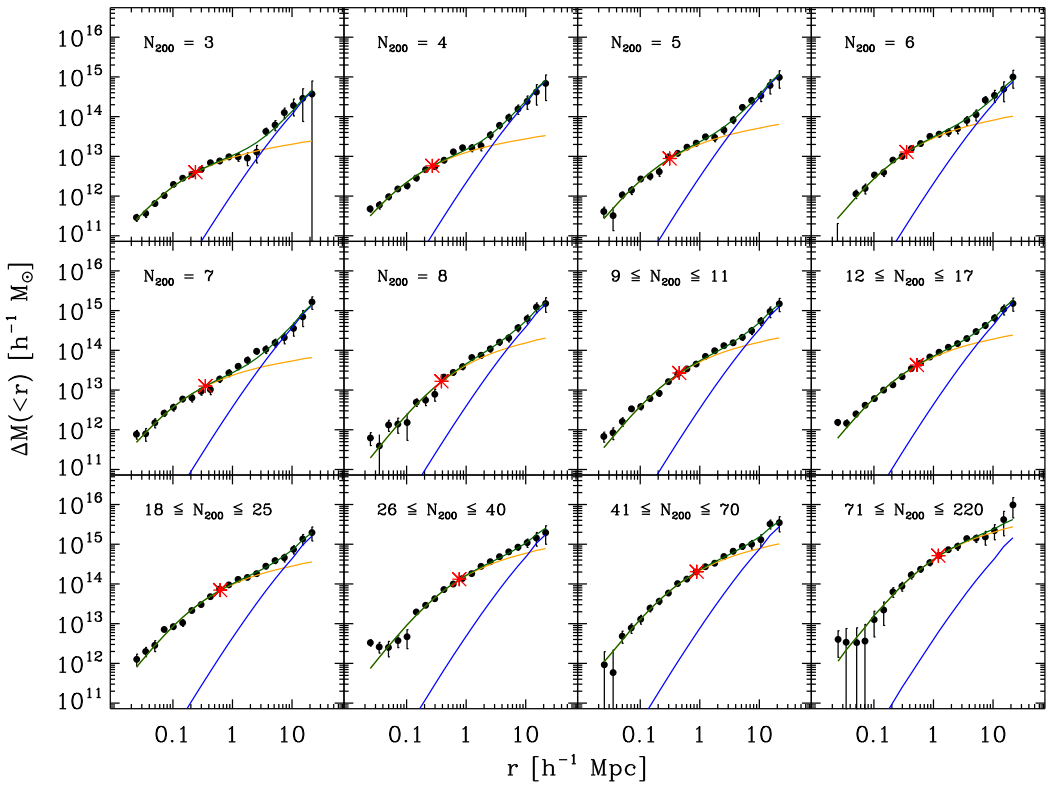

FIG. 7.— Cumulative 3D excess mass profiles for each cluster N_{200} bin derived from weak gravitational lensing. The solid curves show the best fit NFW+linear bias model. The asterisk marks the r_{200}^{mass}. Note these models do not account for possible mis-centering relative to the halo mass peak. They are cluster masses not halo masses.

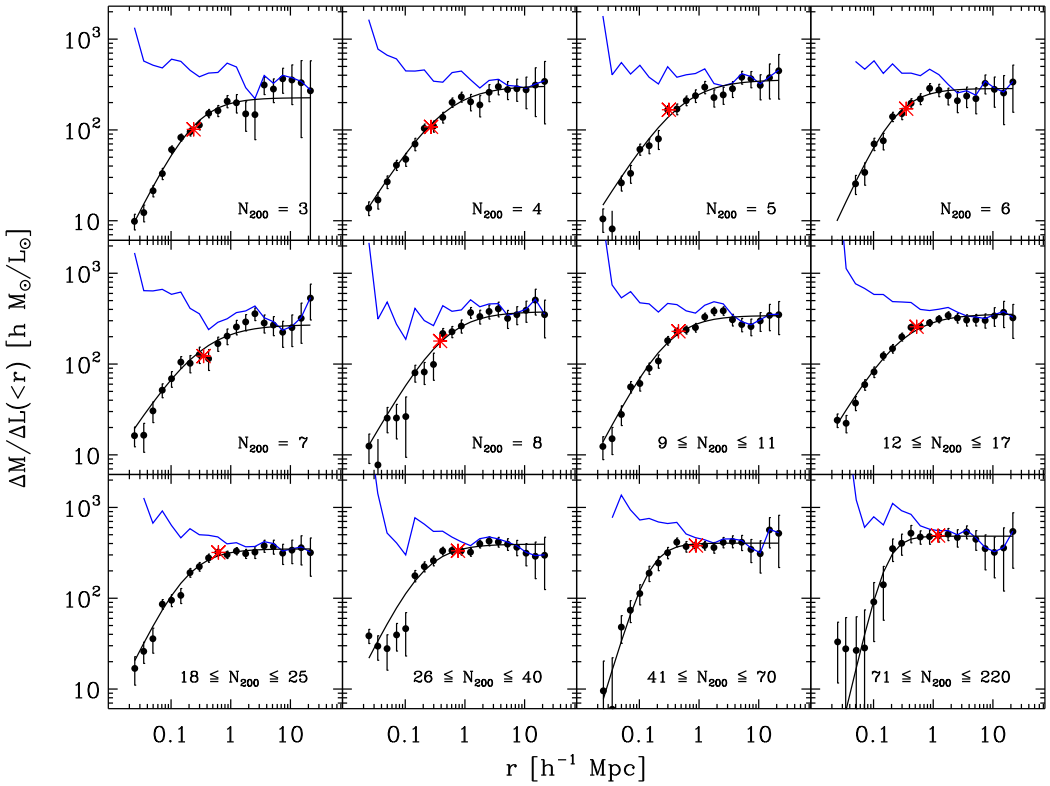

FIG. 8.— Excess mass to excess light ratio profiles for each of the N_{200} bins. These curves are the ratio of the curves shown in Figures 6 and 7. The points with error bars include the mean BCG luminosity. This luminosity is excluded in the upper curve. The asterisk marks r_{200}^{mass}. The curve through the points with error bars is a simple descriptive model as discussed in §9.6.

mean $\Delta M/\Delta L$ within r_{200}^{mass} is a strong function of cluster richness. However, the asymptotic $\Delta M/\Delta L$ is nearly independent of cluster richness.

Without the mean BCG luminosity included, the $\Delta M/\Delta L$ is relatively flat on intermediate to large scales, indicating that the relative amount of mass and light on those scales is not a strong function of radius. There is a turn up at small scales, however. This is partly due to the fact that we do not measure light on scales less than $25h^{-1}$kpc. However, there is also light not counted in our luminosity measurements. It is known that there is a significant amount of intra-cluster light (ICL), light not associated with galaxies, in many clusters (e.g Gonzalez, Zabludoff, & Zaritsky 2005). There is also missing light from galaxies below the luminosity threshold $10^{9.5}h^{-2}L_{\odot}$ and the light not counted from the outskirts of detected galaxies (probably dominated by the outskirts of the BCG on these scales). Only by estimating this missing light will we know the true M/L profile on small scales, and the absolute M/L for all excess light in these clusters. In a future work we will determine this missing luminosity for a subset of the MaxBCG sample presented here.

In order to more quantitively describe the shape of the $\Delta M/\Delta L$ curves, we use a simple fitting function that captures the main features of our profiles. It is a function which would describe the ratio of two equal-index power laws in mass and light plus a delta function for the mean BCG luminosity.

$$\Delta M/\Delta L(<r) = \frac{M_0(r/1h^{-1}\mathrm{Mpc})^{\alpha}}{\langle L_{BCG}\rangle + L_0(r/1h^{-1}\mathrm{Mpc})^{\alpha}} = \left(\frac{(r/r_{1/2})^{\alpha}}{1+(r/r_{1/2})^{\alpha}}\right)\left(\frac{\Delta M}{\Delta L}\right)_{asym}, \quad (19)$$

where $r_{1/2} = (\langle L_{BCG}\rangle/L_0)^{1/\alpha}$ is the radius at which the $\Delta M/\Delta L$ reaches half its asymptotic value at infinity $(\Delta M/\Delta L)_{asym}$. A higher $r_{1/2}$ at fixed α implies a larger fraction of the total light is in the BCG, which results in a slower transition to the asymptotic $\Delta M/\Delta L$.

Although we know the mass and light profiles are not pure power laws, they tend to deviate from a power law in similar ways, which partially cancels this error. However, this means that α should not be interpreted as the slope of the mass or light profile.

The best fits for equation 19 are over-plotted in Figure 8 for the N_{200} binning. We use the full covariance matrix of the $\Delta M/\Delta L$, generated from the covariance matrices of ΔM and ΔL, for the fits. Using the covariance matrix accounts for the strong correlations in the errors caused by the radial integration. The best-fit $r_{1/2}$, α, and $(\Delta M/\Delta L)_{asym}$ are listed in Tables 1 and 2. There is a weak trend of decreasing $r_{1/2}$ with N_{200}, while α is relatively constant except for the highest richness bins. Recall that $r_{1/2} = (\langle L_{BCG}\rangle/L_0)^{1/\alpha}$, and thus a smaller $r_{1/2}$ at fixed α is indicative of a less dominant BCG relative to the overall cluster luminosity, which we had already seen to be true in Figure 6. However, at high masses the value of α increases also, weakening the change in $r_{1/2}$ somewhat. We will discuss the $(\Delta M/\Delta L)_{asym}$ values in section 9.8.

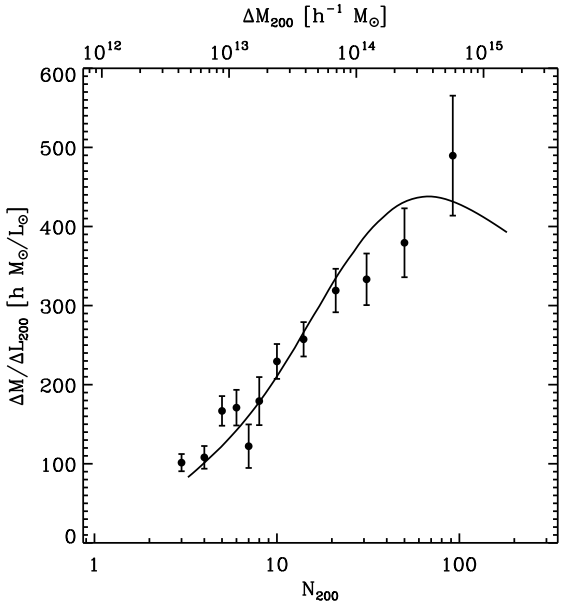

FIG. 9.— The mean $\Delta M/\Delta L$ within r_{200}^{mass} as a function of N_{200}. The mean ΔM_{200} within r_{200}^{mass} centered on BCGs is shown on the top axis, although this is only rough since the transformation between N_{200} and mass is non-linear. No correction for mis-centering of the BCGs relative to the halo mass peaks is included. The $(\Delta M/\Delta L)_{200}$ vs ΔM_{200} is a good fit to a power law with index 0.33 ± 0.02; the $(\Delta M/\Delta L)_{200}$ vs N_{200} is not a good power law. The over-plotted curve is a prediction based on the simulations of Tinker et al. (2005), rescaled in the normalization and mass to pass over the points. This curve is not correctly matched to this data, but is rather intended to show the rough expected trend with mass.

9.7. *Mass-to-light Ratio Within r_{200}^{mass}*

In Figure 9 we show the mean $\Delta M/\Delta L$ within r_{200}^{mass}, $(\Delta M/\Delta L)_{200}$, for each of the cluster richness and luminosity bins, plotted as a function of the mean N_{200}. The $\Delta M/\Delta L$ increases strongly with N_{200} over two orders of magnitude in mass. The ΔM_{200} is also shown on the top axis, but note this is rough as the transformation is non-linear. The $(\Delta M/\Delta L)_{200}$ versus ΔM_{200} is a good fit to a power law with index 0.33 ± 0.02. The $(\Delta M/\Delta L)_{200}$ vs. N_{200}, however, is not a good fit to a power law.

As we mentioned in §9.5, we have taken no account of the possible mis-centering of the BCGs relative to the underlying halo centers or peaks. The measurements as presented have the advantage of being non-parametric, but the interpretation is more difficult. A fully model-dependent analysis for both the mass and light profiles following Johnston et al. (2007b) may imply different results for $(\Delta M/\Delta L)_{200}$ measured around dark matter halos than those around MaxBCG clusters.

Over-plotted in Figure 9 is a prediction from Tinker et al. (2005) for $z = 0$ rest-frame r-band light rather than ${}^{0.25}i$, and M_{180} mean rather than M_{200} crit. The axes have been scaled arbitrarily so the curve passes over the points. We do not expect this prediction to match our data, which is in a different band, uses a different mass estimator, and for which there are mis-centering effects. The point here is to show a rough expected trend with mass. There is qualitative agreement with the mass scaling of this prediction and our data.

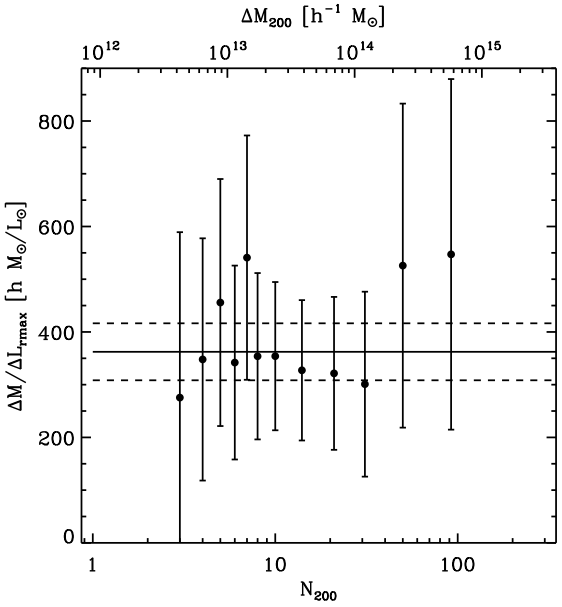

FIG. 10.— Asymptotic excess mass-to-light ratio as a function of N_{200}. This is simply the last point on the integrated $\Delta M/\Delta L$ curve at $r = 22h^{-1}$Mpc. The mean ΔM within r_{200}^{mass} centered on BCGs is shown on the top axis, although this is only rough since the transformation between N_{200} and mass is non-linear. The mean $\Delta M/\Delta L = 349 \pm 51h$, averaged over all samples, is plotted as the horizontal line

9.8. *Asymptotic Mass-to-light Ratio*

The $\Delta M/\Delta L$ profiles shown in Figure 8 rise quickly and flatten at large separations. We measure this asymptotic value in two separate ways. First we use the last point in the $\Delta M/\Delta L$ curve at $r < 22h^{-1}$Mpc, which we will refer to as $(\Delta M/\Delta L)_{22\mathrm{Mpc}}$. The $(\Delta M/\Delta L)_{22\mathrm{Mpc}}$ for each richness bin is shown in Figure 10. Note, the value at $22h^{-1}$Mpc should be insensitive to any possible mis-centering of the BCGs relative to the true halo mass peak. We detect no trend in the $(\Delta M/\Delta L)_{22\mathrm{Mpc}}$ as a function of N_{200}. For the average value we get $362 \pm 54h$ for the richness binning and $349 \pm 51h$ for the luminosity binning. Note these are not independent measures since the same clusters are used for both binnings.

For the second method we examine the $(\Delta M/\Delta L)_{asym}$ values measured from the fits in §9.6, which are listed in Tables 1 and 2. As with the $(\Delta M/\Delta L)_{22\mathrm{Mpc}}$ values, they are roughly constant with N_{200}. The average values are $357 \pm 9h$ for the richness binning and $335 \pm 9h$ for the luminosity binning. Note the two binnings are not independent measures as the same clusters are used for both. Both are consistent with the values we get just taking the last point $(\Delta M/\Delta L)_{22\mathrm{Mpc}}$.

10. DISCUSSION

The integrated $\Delta M/\Delta L$ around MaxBCG clusters has a generic form. At $25h^{-1}$kpc, where the light of the cluster is dominated by the BCG, the $\Delta M/\Delta L$ is $\sim 10h^{-2}M_\odot/L_\odot$. There is a sharp rise and then the profile flattens out at large scales ($22h^{-1}$Mpc). We fit a simple model to extract $r_{1/2}$, the radius at which the $\Delta M/\Delta L$ reaches half its value at infinity.

For $M_{200} < 10^{14}M_\odot$, $r_{1/2}$ is determined primarily by the relative amount of light in the BCG compared to the rest of the cluster. For higher masses the $\Delta M/\Delta L$ asymptotes to $(\Delta M/\Delta L)_{asym}$ more quickly relative to the lower masses, resulting in a smaller $r_{1/2}$.

The decreasing $r_{1/2}$ with richness is partly due to the less dominant BCGs for higher richness clusters; the effect of the BCG on the integrated light is only important on small scales for very richness systems. But it is also partly because the measured $\Delta M/\Delta L$ within the large clusters is closer to the asymptotic value in the interiors of these systems. Figure 8 indicates that the $\Delta M/\Delta L$ not including the BCG light is more flat for the high richness clusters that have especially sharp transitions. The $\Delta M/\Delta L$ would be essentially equal to $(\Delta M/\Delta L)_{asym}$ if it were not for the presence of the BCG. This is not true for the lower richness systems.

This difference between high and low richness systems leads us back to the discussion of missed light. By missed light we simply mean any light not counted in our measurements. This uncounted light is partly intracluster light (ICL), light not associated with galaxies. There is also light from galaxies less luminous than the threshold $10^{9.5}h^{-2}L_\odot$. The total luminosity of galaxies below this threshold is probably not dominant, and the radial profile is probably similar to that of galaxies above the threshold, so including it would not change the profile dramatically. But the ICL has a steeper profile. It appears to follow a $\exp(-r^{1/4})$ law, with scale length of order 100 h^{-1} kpc, and contains many times more light than the BCG (Gonzalez et al. 2005). The total light in this component scales slowly with richness, and is more dominant in smaller systems on small scales. This could explain what appears to be a slower rise in $\Delta M/\Delta L$ relative to larger systems. We will explore the ICL for MaxBCG clusters in a future paper.

The $(\Delta M/\Delta L)_{200}$, the excess mass-to-light within r_{200}^{mass}, scales with richness and M_{200}. For lower richness systems, the $(\Delta M/\Delta L)_{200}$ is considerably smaller than $(\Delta M/\Delta L)_{asym}$, while for larger systems it is of order $(\Delta M/\Delta L)_{asym}$. This trend is probably a reflection of both a true difference in mean $\Delta M/\Delta L$ and the effect of the ICL, which may be more dominant for lower mass systems. The $(\Delta M/\Delta L)_{200}$ versus N_{200} is not a good fit to a power law, but $(\Delta M/\Delta L)_{200}$ versus ΔM_{200} does is well fit by a power law with index 0.33 ± 0.02. However, no attempt was made to model mis-centering of BCGs relative to halo mass peaks. The $\Delta M/\Delta L$ will not be strongly affected because the luminosity roughly traces mass, the ΔM_{200} as a function of N_{200} does change significantly (Johnston et al. 2007b).

It is difficult to compare with the literature due to the many conventions in use, such as lower luminosity thresholds, galaxy aperture definitions, mass apertures, projected vs. de-projected masses, background subtracted luminosities or not, as well as the various bandpasses used for the exposures. See below for comparisons of the Ω_m calculated from the inferred global mass-to-light ratio, which may be less dependent on these factors.

We used two methods to extract the asymptotic $\Delta M/\Delta L$: the value with in $22h^{-1}$Mpc, $(\Delta M/\Delta L)_{22\mathrm{Mpc}}$, and the best-fit value from our fitting function, $(\Delta M/\Delta L)_{asym}$. Note, on these large scales, any mis-centering of the BCGs relative to the halo mass peak is irrelevant. We see no trend of either measure of the asymptotic $\Delta M/\Delta L$ with N_{200}.

As we discussed in the introduction, for any given cluster sample, the asymptotic $\Delta M/\Delta L$ is proportional to the mass-to-light ratio of the universe. Repeating equation 2 here for clarity:

$$(\Delta M/\Delta L)_{asym} = \langle M/L \rangle \; b_{M/L}^{-2}$$
$$b_{M/L}^{-2} = \frac{b_{cm}}{b_{c\ell}} \frac{1}{b_{\ell m}^2}.$$

where $b_{M/L}^2$ depends primarily on the bias of the galaxy tracers relative to the underlying mass distribution, since the bias of the clusters likely cancels out in $b_{cm}/b_{c\ell}$.

Thus, if the bias $b_{M/L}^2$ is independent of cluster richness, then the lack of a trend of $(\Delta M/\Delta L)_{22\mathrm{Mpc}}$ with N_{200} means we have measured the same asymptotic $\Delta M/\Delta L$ for all richness bins. If $b_{M/L}^2$ is not independent of N_{200}, then by chance the variations in asymptotic $\Delta M/\Delta L$ were canceled by a corresponding change in the bias. So we need to determine whether this bias is constant.

The bias $b_{M/L}^2$ should primarily depend on the mass of the halos hosting the light tracers, and this should be related to the luminosity of those galaxies. Included in the Tables 1 and 2 is the mean i-band luminosity of galaxies at $10h^{-1}$ Mpc separations $\langle L_{10}^{gal} \rangle$. The value on larger scales was not well constrained for all richness bins. There is not a strong variation of this mean luminosity between the richness bins. The average, over all cluster richness bins, of the luminosity of galaxies within 10Mpc is $L_{^{0.25}i} = (1.10 \pm 0.04) \times 10^{10} h^{-2} L_\odot$ $(-20.43 \pm 0.04$ mag). Note in §7 we saw that $L^*_{^{0.25}i} = 1.7 \times 10^{10}$. Given the small variation in luminosity, and the fact that the bias varies quite slowly for $L < L_*$ galaxies (Tegmark et al. 2004), the bias $b_{M/L}^2$ should be roughly constant for each cluster sample. Thus we will assume we are measuring the true asymptotic value at large separations, and average these values from all cluster richness bins.

In section 9.8 we calculated this asymptotic value in two ways: first by taking the value of the integrated $\Delta M/\Delta L$ for the last radial bin $22h^{-1}$Mpc to get $(\Delta M/\Delta L)_{22\mathrm{Mpc}}$, and the second fitting a simple descriptive model to get $(\Delta M/\Delta L)_{asym}$. Averaging over all cluster luminosity bins gives

$$\langle M/L \rangle \; b_{M/L}^{-2} = \begin{cases} 362 \pm 54h & \text{within } 22h^{-1}\mathrm{Mpc} \\ 357 \pm 9h & \text{asymptotic fit} \end{cases} \quad (20)$$

in solar units, where the bias $b_{M/L}^2$ corresponds to that of $L_{^{0.25}i} = 1.10 \times 10^{10} h^{-2} \mathrm{L}_\odot$ galaxies at z=0.25.

In §7 we calculated that the luminosity density in the $^{0.25}i$-band is $(3.14 \pm 0.10) \times 10^8 \; h \; L_\odot \mathrm{Mpc}^{-3}$. Multiplying the asymptotic M/L above by this, and dividing by the critical density, number we get an estimate of Ω_m that is independent of h:

$$\Omega_m b_{M/L}^{-2} = \begin{cases} 0.20 \pm 0.03 & \text{within } 22h^{-1}\mathrm{Mpc} \\ 0.194 \pm 0.008 & \text{asymptotic fit} \end{cases} \quad (21)$$

There is certainly more information than we have used in the $22h^{-1}$Mpc values since points at smaller radius do contain independent information. So in principle a more precise measurement could be made, but the error within $22h^{-1}$Mpc can be considered conservative. On the other hand, the error bar on the asymptotic fit is certainly an underestimate, as the fit is not based on a physical model; this error should be thought of as a lower limit.

In addition there is a level of systematic error not accounted for here. Although the level of systematic error is not precisely known, we expect it to be $\lesssim 10\%$, mostly due to errors in photometric redshifts of lensing source galaxies. See Johnston et al. (2007b) for a more complete discussion of systematic errors.

There have been numerous studies measuring mass-to-light ratios of clusters. As discussed above with regards to the $(\Delta M/\Delta L)_{200}$-$M_{200}$ relation, there are a wide variety of techniques and conventions in place. Many of these studies use the mass-to-light ratio to infer Ω_m by assuming the value they get is equal to that of the universe. Although this is not always a well-justified assumption, converting to Ω_m does remove most of the dependence on the bandpass, galaxy apertures, and mass aperture (as long as the mass aperture isn't too small). Using the inferred Ω_m may lead to a more robust comparison between the various results.

The series of papers by Bahcall et al. have consistently gotten $\Omega_m \sim 0.2$ from this technique, using various mass estimators. For example using X–ray clusters (Bahcall & Comerford 2002) found 0.17 ± 0.05 and SDSS clusters whose masses were calibrated from velocity dispersions gave 0.19 ± 0.08 (Bahcall et al. 2003).

Results from velocity dispersions in the CNOC data have also been used to infer Ω_m. Using stacked velocity and B-band light profiles, Carlberg et al. (1997) found $\Omega_m = 0.19 \pm 0.06$. A recent analysis using individual masses and K-band light found 0.22 ± 0.02 Muzzin et al. (2007).

Using the "caustic" method for estimating masses and K-band light in the CAIRNS survey, Rines et al. (2004) inferred $\Omega_m = 0.18 \pm 0.03$. This method claims to yield more accurate masses by correctly modeling the infall regions around clusters. The study by Hoekstra et al. (2001) using weak lensing for group masses and B-band light found $\Omega_m = 0.13 \pm 0.07$. It should be noted that these are rather small groups; as we have shown in this work the mass-to-light ratio is less than universal within their virial radii. Using X–ray data for a set of 2MASS clusters, and 2MASS K-band luminosities, Lin et al. (2003) find $\Omega_m = 0.19 \pm 0.03$.

Although there is general agreement when using mass-to-light ratios to infer Ω_m, these measurements give smaller values for Ω_m than baryon fraction measurements, although baryon fraction measurements do have dependence on h. This is noted, for example, by Lin et al. (2003) where they find a higher $\Omega_m = 0.28 \pm 0.03$ using the baryon fraction using their own data, and suggest their mass-to-light ratios are too low.

In our analysis, we have found that the mass-to-light ratioi reaches an asymptotic value at large radius. The missed light, ICL and otherwise, will generally push the mass-to-light ratios even lower. It is possible, however, that the $b_{M/L}^2$ is considerably greater than unity. This is not the theoretical expectation, however, since the light tracers are $L < L_*$ galaxies which should reside in underbiased halos (Sheth & Tormen 1999; Seljak & Warren 2004).

Note we have assumed a fiducial flat cosmology with

$\Omega_m = 0.27$ when performing these measurements, and this has not been varied properly in order to constrain Ω_m above. Thus the calculated Ω_m could be slightly biased, and there could be some additional statistical error not accounted for here. But at these redshifts such effects should be secondary. In a future paper we will present a full cosmological analysis including these effects as well as a proper model for BCG displacements from the halo mass peak as carried out in Johnston et al. (2007b).

These results are a precise test for models of structure and galaxy formation. The M/L results, coupled with the galaxy color and luminosity distributions as a function of radius from clusters (sections 9.1 and 9.3) tell us in detail how different types of galaxies are distributed in and around these clusters and how they are clustered relative to the underlying mass distribution (see also Hansen et al. 2007). These are the most basic cross-correlation statistics that can be addressed, and are perhaps the most precise and powerful statistics that can be measured by a photometric survey.

It is significant that these measurements were carried out in a purely photometric data set. Every step of the process uses photometric data only, from cluster finding, to galaxy cross-correlations, to lensing measurements. These type of measurements can be carried out in any high-quality survey with properly chosen bandpasses. Future surveys such as DES, SNAP, and LSST will greatly extend these measurements and further challenge our theories of cosmology and galaxy formation.

E.S. thanks the Aspen Center for Physics and the organizers of the "Modeling Galaxy Clustering" workshop for creating such a productive working environment; most of this paper was written during his two weeks there.

Thanks to David Hogg for many helpful comments. Thanks to Roman Scoccimarro and Mulin Ding for use of the "Mafalda" computing cluster.

E.S. was supported by NSF grant AST-0428465. B.K. and T.A.M. gratefully acknowledge support from NSF grant AST 044327 and the Michigan Center for Theoretical Physics

The research described in this paper was performed in part at the Jet Propulsion Laboratory, California Institute of Technology, under a contract with the National Aeronautics and Space Administration.

Funding for the SDSS and SDSS-II has been provided by the Alfred P. Sloan Foundation, the Participating Institutions, the National Science Foundation, the U.S. Department of Energy, the National Aeronautics and Space Administration, the Japanese Monbukagakusho, the Max Planck Society, and the Higher Education Funding Council for England. The SDSS Web Site is http://www.sdss.org/.

The SDSS is managed by the Astrophysical Research Consortium for the Participating Institutions. The Participating Institutions are the American Museum of Natural History, Astrophysical Institute Potsdam, University of Basel, Cambridge University, Case Western Reserve University, University of Chicago, Drexel University, Fermilab, the Institute for Advanced Study, the Japan Participation Group, Johns Hopkins University, the Joint Institute for Nuclear Astrophysics, the Kavli Institute for Particle Astrophysics and Cosmology, the Korean Scientist Group, the Chinese Academy of Sciences (LAMOST), Los Alamos National Laboratory, the Max-Planck-Institute for Astronomy (MPIA), the Max-Planck-Institute for Astrophysics (MPA), New Mexico State University, Ohio State University, University of Pittsburgh, University of Portsmouth, Princeton University, the United States Naval Observatory, and the University of Washington.

REFERENCES

Adelman-McCarthy, J. K. et al. 2006, ApJS, 162, 38
Bahcall, N. A. & Comerford, J. M. 2002, ApJ, 565, L5
Bahcall, N. A. et al. 2003, ApJ, 585, 182
Becker, M. R. et al. 2007, ArXiv e-prints, 704
Blanton, M. R. 2006, ApJ, 648, 268
Blanton, M. R. & Roweis, S. 2007, AJ, 133, 734
Blanton, M. R. et al. 2003a, AJ, 125, 2348
—. 2003b, ApJ, 592, 819
—. 2005, AJ, 129, 2562
Carlberg, R. G., Yee, H. K. C., & Ellingson, E. 1997, ApJ, 478, 462
Clowe, D., Bradač, M., Gonzalez, A. H., Markevitch, M., Randall, S. W., Jones, C., & Zaritsky, D. 2006, ApJ, 648, L109
Clowe, D., Luppino, G. A., Kaiser, N., & Gioia, I. M. 2000, ApJ, 539, 540
Cunha, C., Oyaizu, H., Lima, M., Lin, H., & Frieman, J. 2007, in preparation
Dahle, H. ., Kaiser, N., Irgens, R. J., Lilje, P. B., & Maddox, S. J. 2002, ApJS, 139, 313
Evrard, A. E. et al. 2002, ApJ, 573, 7
Fahlman, G., Kaiser, N., Squires, G., & Woods, D. 1994, ApJ, 437, 56
Fischer, P. & Tyson, J. A. 1997, AJ, 114, 14
Gonzalez, A. H., Zabludoff, A. I., & Zaritsky, D. 2005, ApJ, 618, 195
Hansen, S. et al. 2007, in preparation
Hansen, S. M., McKay, T. A., Wechsler, R. H., Annis, J., Sheldon, E. S., & Kimball, A. 2005, ApJ, 633, 122
Heitmann, K. et al. 2007, ArXiv e-prints, 706
Hoekstra, H., Franx, M., Kuijken, K., & Squires, G. 1998, ApJ, 504, 636
Hoekstra, H. et al. 2001, ApJ, 548, L5
Hubble, E. P. 1929, ApJ, 69, 103
Joffre, M. et al. 2000, ApJ, 534, L131
Johnston, D. E. et al. 2007a, ApJ, 656, 27
—. 2007b, in preparation
Kapteyn, J. C. 1922, ApJ, 55, 302
Koester, B. P. et al. 2007a, ApJ, 660, 221
—. 2007b, ApJ, 660, 239
Lin, Y.-T., Mohr, J. J., & Stanford, S. A. 2003, ApJ, 591, 749
—. 2004, ApJ, 610, 745
Luppino, G. A. & Kaiser, N. 1997, ApJ, 475, 20
Mandelbaum, R. et al. 2005, MNRAS, 361, 1287
Masjedi, M. et al. 2006, ApJ, 644, 54
Massey, R. et al. 2006, in preparation
Muzzin, A., Yee, H. K. C., Hall, P. B., & Lin, H. 2007, ApJ, 663, 150
Navarro, J. F., Frenk, C. S., & White, S. D. M. 1997, ApJ, 490, 493+
Parker, L. C., Hudson, M. J., Carlberg, R. G., & Hoekstra, H. 2005, ApJ, 634, 806
Plummer, H. C. 1911, MNRAS, 71, 460
Rines, K., Geller, M. J., Diaferio, A., Kurtz, M. J., & Jarrett, T. H. 2004, AJ, 128, 1078
Rozo, E., Wechsler, R. H., Koester, B. P., Evrard, A. E., & McKay, T. A. 2007a, ArXiv Astrophysics e-prints
Rozo, E., Wechsler, R. H., Koester, B. P., McKay, T. A., Evrard, A. E., Johnston, D., Sheldon, E. S., Annis, J., & Frieman, J. A. 2007b, ArXiv Astrophysics e-prints
Schlegel, D. J., Finkbeiner, D. P., & Davis, M. 1998, ApJ, 500, 525+
Schmidt, M. 1968, ApJ, 151, 393
Scranton, R. et al. 2002, ApJ, 579, 48
Seljak, U. & Warren, M. S. 2004, MNRAS, 355, 129
Sheldon, E. S. et al. 2001, ApJ, 554, 881
—. 2007, in preparation
Sheth, R. K. & Tormen, G. 1999, MNRAS, 308, 119
Tegmark, M. et al. 2004, Submitted to ApJ
Tinker, J. L., Weinberg, D. H., Zheng, Z., & Zehavi, I. 2005, ApJ, 631, 41
Tyson, J. A. & Fischer, P. 1995, ApJ, 446, L55+
Umetsu, K., Broadhurst, T., Takada, M., & Kong, X. 2005, Journal of Korean Astronomical Society, 38, 191
Wechsler, R. et al. 2008, in preparation
Wittman, D., Margoniner, V. E., Tyson, J. A., Cohen, J. G., Becker, A. C., & Dell'Antonio, I. P. 2003, ApJ, 597, 218
York, D. G. et al. 2000, AJ, 120, 1579
Zehavi, I. et al. 2005, ApJ, 630, 1
Zwicky, F. 1933, Helvetica Physica Acta, 6, 110
—. 1937, ApJ, 86, 217+